



ARL-TR-7428 • SEP 2015



A New Semi-Implicit Time Integration Scheme for the Time-Dependent Atmospheric Boundary Layer Environment (ABLE) Model

by Benjamin T MacCall, Yansen Wang, and Wen-Yih Sun

Approved for public release; distribution unlimited.

NOTICES

Disclaimers

The findings in this report are not to be construed as an official Department of the Army position unless so designated by other authorized documents.

Citation of manufacturer's or trade names does not constitute an official endorsement or approval of the use thereof.

Destroy this report when it is no longer needed. Do not return it to the originator.



A New Semi-Implicit Time Integration Scheme for the Time-Dependent Atmospheric Boundary Layer Environment (ABLE) Model

by Benjamin T MacCall and Yansen Wang
Computational and Information Sciences Directorate, ARL

Wen-Yih Sun
Purdue University

REPORT DOCUMENTATION PAGE				Form Approved OMB No. 0704-0188	
<p>Public reporting burden for this collection of information is estimated to average 1 hour per response, including the time for reviewing instructions, searching existing data sources, gathering and maintaining the data needed, and completing and reviewing the collection information. Send comments regarding this burden estimate or any other aspect of this collection of information, including suggestions for reducing the burden, to Department of Defense, Washington Headquarters Services, Directorate for Information Operations and Reports (0704-0188), 1215 Jefferson Davis Highway, Suite 1204, Arlington, VA 22202-4302. Respondents should be aware that notwithstanding any other provision of law, no person shall be subject to any penalty for failing to comply with a collection of information if it does not display a currently valid OMB control number.</p> <p>PLEASE DO NOT RETURN YOUR FORM TO THE ABOVE ADDRESS.</p>					
1. REPORT DATE (DD-MM-YYYY) Sep 2015		2. REPORT TYPE Final		3. DATES COVERED (From - To)	
4. TITLE AND SUBTITLE A New Semi-Implicit Time Integration Scheme for the Time-Dependent Atmospheric Boundary Layer Environment (ABLE) Model				5a. CONTRACT NUMBER	
				5b. GRANT NUMBER	
				5c. PROGRAM ELEMENT NUMBER	
6. AUTHOR(S) Benjamin T MacCall, Yansen Wang, and Wen-Yih Sun				5d. PROJECT NUMBER	
				5e. TASK NUMBER	
				5f. WORK UNIT NUMBER	
7. PERFORMING ORGANIZATION NAME(S) AND ADDRESS(ES) US Army Research Laboratory ATTN: RDRL-CIE-M 2800 Powder Mill Road Adelphi, MD 20783-1138				8. PERFORMING ORGANIZATION REPORT NUMBER ARL-TR-7428	
9. SPONSORING/MONITORING AGENCY NAME(S) AND ADDRESS(ES)				10. SPONSOR/MONITOR'S ACRONYM(S)	
				11. SPONSOR/MONITOR'S REPORT NUMBER(S)	
12. DISTRIBUTION/AVAILABILITY STATEMENT Approved for public release; distribution unlimited					
13. SUPPLEMENTARY NOTES					
14. ABSTRACT <p>The time integration scheme demonstrated for the nonlinear shallow water equations has been extended to the 3-dimensional Navier-Stokes system and implemented as a time-dependent, finite-volume, convection-diffusion scheme in a new direct numerical simulation code. The model was compared with other simulation and laboratory results of lid-driven cavity flows with Reynolds numbers of $Re=1000$, 3200, and 10,000 to assess simulation of boundary forced flows and generation of intermittent flow structures. The generation and shedding of the various flow vortices, including Taylor-Goertler like (TGL) vortices, impact the velocity variances and covariance as observed, though the vortex shedding frequency is greater than observed in the laboratory. The scheme's low implicit diffusion, reduced need for explicit smoothing, and straightforward parallel implementation make it a good candidate for incorporating into finite-volume, large-eddy simulation for highly time-dependent atmospheric boundary layer flow.</p>					
15. SUBJECT TERMS direct numerical simulation; semi-implicit time integration scheme; lid-driven cavity flow; three-dimensional, finite-volume scheme; Taylor-Goertler like vortices					
16. SECURITY CLASSIFICATION OF:			17. LIMITATION OF ABSTRACT UU	18. NUMBER OF PAGES 28	19a. NAME OF RESPONSIBLE PERSON Benjamin T McCall
a. REPORT Unclassified	b. ABSTRACT Unclassified	c. THIS PAGE Unclassified			19b. TELEPHONE NUMBER (include area code) 301-394-1463

Contents

List of Figures	iv
Acknowledgments	vi
1. Introduction	1
2. Methodology	2
3. Results	5
3.1 Discretization Error	5
3.2 Comparison with Simulation and Observations	8
4. Conclusion	16
5. References	18
List of Symbols, Abbreviations, and Acronyms	19
Distribution List	20

List of Figures

Fig. 1	Diagram of lid-driven cavity flow and associated flow structures. The upper boundary of the box is moving with a velocity of U_0 in the positive x-direction. All boundaries are no-slip. Adapted from Shankar and Deshpande (2000).	2
Fig. 2	Arakawa C-grid configuration in the xy-plane for the scalar mass field and the U- and V-components of the momentum field. The vertical momentum is staggered in the vertical direction from the mass field points.....	4
Fig. 3	Estimate of temporal discretization error based on lid-driven cavity flow simulations with $Re=10,000$. The largest time step satisfied the CFL criterion for the reduced speed acoustic waves. Additional simulations were performed using an identical grid, but with time steps reduced by factors of 1/2, 1/4, and 1/8, which was used as the reference state.	6
Fig. 4	Spatial discretization error estimates using stream-wise and vertical velocities in the plane of symmetry ($y=0$) for $Re=1000$. The error is the L_2 -norm of the variable difference from a reference simulation that used 450 grid points in each direction. For a) the error is calculated over the entire symmetry plane and for b) 20% of each side of the symmetry plane is excluded.....	7
Fig. 5	a) Stream-wise velocity along the central vertical axis and b) vertical velocity along the central horizontal axis for $Re=1000$. The model simulations used 75, 150, 300, and 450 grid points in each direction and are compared with the simulations of Ku, Hirsh, and Taylor (1987).	9
Fig. 6	Streamlines and UW-velocity magnitudes ($Re=3200$) showing a) at $t = 90\tau$, a well-defined DSE and localized downstream flow along the right, boundary; b) at $t = 93\tau$, the shedding of the DSE raising the level that the downstream maximum wraps around the PE; c) at $t = 97\tau$, drop and acceleration of the downstream flow; and d) at $t = 104\tau$, reestablishment of the DSE and thinning of the downstream maximum.	11
Fig. 7	Non-dimensional mean horizontal and vertical velocity fields along the x- and z-axes in the symmetry plane ($y=0$) for a) $Re=3200$ and b) $Re=10,000$	12
Fig. 8	Scaled horizontal and vertical velocity variances along the x- and z-axes in the symmetry plane ($y=0$) for a) $Re=3200$ and b) $Re=10,000$.	13
Fig. 9	Scaled horizontal and vertical velocity covariances along the central axes in the symmetry plane ($y=0$) for a) $Re=3200$ and b) $Re=10,000$.	14

Fig. 10	Streamline and VW-velocity magnitudes for the same times shown in Fig. 6 a) $t = 90\tau$, b) $t = 93\tau$, c) $t = 97\tau$, and d) $t = 104\tau$. This progression of figures shows the meandering of the TGL vortices near the symmetry plane ($Y^*=0$).	15
Fig. 11	Streamlines and VW-velocity magnitude for $Re=10,000$ at time, $t = 110\tau$. For the higher- Re flow the vortices generated near the lower boundary are irregular and transient.	16

Acknowledgments

The High-Performance Computing Modernization Office (HPCMO) and the Defense Shared Resource Centers (DSRC) at the US Army Research Laboratory and Naval Research Laboratory supported this project with computational resources.

1. Introduction

Sun (2011) introduced a new semi-implicit, time integration scheme and simulated solutions to the cylindrical dam-break problem for the nonlinear shallow water equations. The scheme exhibited several important benefits relating to the overall stability of the integration and preservation of strong gradients in the calculated flow quantities. The integration reproduced the solutions of Godunov-type Riemann solvers comparing favorably to more sophisticated and more computationally intensive schemes. The new scheme is a 2-time-step scheme similar in structure to the forward-backward finite-difference scheme (Haltiner and Williams 1980). Thus, there is no computational mode, and incorporating a split-time-step scheme in order to less frequently update slowly varying quantities will not require any time filtering (Hsu and Sun 2001). As part of the linear stability analysis, Sun (2011) showed that the scheme has a diffusion term similar to the Lax-Wendroff scheme; however, based on eigenvalue analysis, the amplification factor is unity for Courant numbers less than 1.

Here we apply the scheme to the 3-dimensional (3-D) Navier-Stokes equations as a module in the Atmospheric Boundary Layer Environment (ABLE) model (Wang et al. 2012), a new computational fluid dynamics (CFD) model code in development at the US Army Research Laboratory. The model is being developed for eventual application to atmospheric, planetary boundary layer (PBL) flows in complex and urban terrain. Accurate simulation within the PBL necessarily includes producing fine-scale structures (e.g., thermal plumes in convective conditions [Moeng and Sullivan 1994], shear-layers [Chimonas 1999], and terrain-induced vortex shedding/generation in stable conditions [Grubisic et al. 2008]), and excessive numerical diffusion may compromise their formation or severely degrade their evolution compared to observations.

The new semi-implicit scheme was implemented as an option for the ABLE model's dynamical core (version 0.90). In order to characterize the scheme's performance, we simulated a 3-D lid-driven cavity flow (reviewed in Shankar and Deshpande [2000]) and compared the results simulations of Ku et al. (1987) and the laboratory measurements of Prasad and Koseff (1989). Lid-driven cavity flow is commonly used to evaluate numerical schemes because of the unambiguous boundary conditions, the detailed laboratory observations of Prasad and Koseff (1989), and features such as the intermittent and semi-permanent vortex structures shown in Fig. 1 (Shankar and Deshpande 2000).

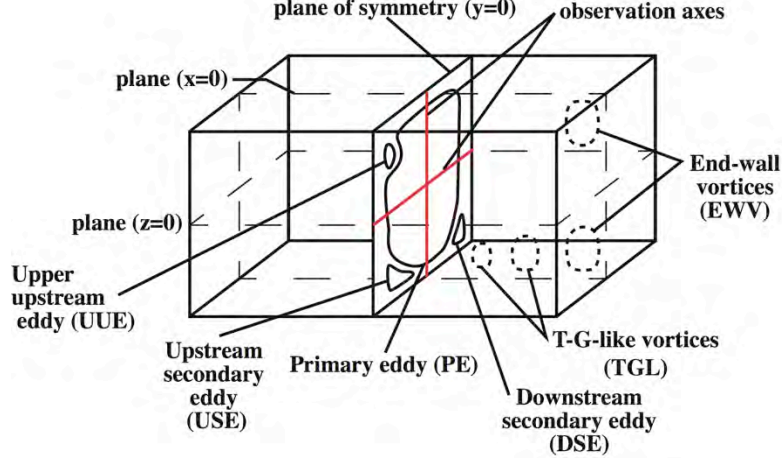


Fig. 1 Diagram of lid-driven cavity flow and associated flow structures. The upper boundary of the box is moving with a velocity of U_0 in the positive x -direction. All boundaries are no-slip. Adapted from Shankar and Deshpande (2000).

2. Methodology

The general formulation for the semi-implicit scheme for a set of n prognostic variables, ϕ_i , impacted by forcing functions, \mathcal{F}_i , is

$$\frac{\partial \phi_i}{\partial t} = -\mathcal{F}_i(\phi_1, \dots, \phi_n); \quad i = 1, \dots, n; \quad j = 1, 2, 3. \quad (1)$$

Discretizing the above set of n equations, the semi-implicit scheme calculates the forcing at the midpoint between the 2 time steps, $t = t_0 + \Delta t/2$:

$$\frac{\phi_i(x_j, \Delta t + t_0) - \phi_i(x_j, t_0)}{\Delta t} = -\mathcal{F}_i\left(\phi_1\left(x_j, \frac{\Delta t}{2} + t_0\right), \dots, \phi_n\left(x_j, \frac{\Delta t}{2} + t_0\right)\right); \quad i = 1, \dots, n; \quad j = 1, 2, 3 \quad (2)$$

Approximating the prognostic variables at that midpoint is done using a truncated Taylor expansion with respect to time. The time derivatives in the first-order terms are then replaced by the forcing functions, \mathcal{F}_i , evaluated at $t = t_0$:

$$\begin{aligned} \phi_i\left(x_j, \frac{\Delta t}{2} + t_0\right) &= \phi_i(x_j, t_0) + \frac{\Delta t}{2} \frac{\partial \phi_i(x_j, t)}{\partial t} \Big|_{t=t_0} \\ &= \phi_i(x_j, t_0) + \frac{\Delta t}{2} \mathcal{F}_i(\phi_1(x_j, t_0), \dots, \phi_n(x_j, t_0)) \end{aligned} \quad (3)$$

For the 3-D finite-volume formulation, the prognostic variables are density, ρ , momentum, $U_i = \rho u_i$, and density-coupled potential temperature, $\Theta = \rho \theta$. For the simulations reported below, the model is configured as a direct numerical simulation (DNS). Because the molecular diffusion terms are retained, runs must

be high enough resolution to resolve motions down into the dissipation subrange, where the magnitudes of these diffusion terms become of similar order to the other forcing. Because of the importance of accurately calculating the pressure gradient force in the momentum equations, the thermodynamic variables, ρ and Θ , are updated first. Following the summation convention over repeated indices, the governing equations are

$$\delta \frac{\partial \rho}{\partial t} = - \frac{\partial U_i}{\partial x_i} \quad (4)$$

$$\frac{\partial \Theta}{\partial t} = \kappa \frac{\partial^2}{\partial x_j \partial x_j} \left(\frac{\Theta}{\rho} \right) - \frac{\partial}{\partial x_j} \left(\frac{\Theta U_j}{\rho} \right) \quad (5)$$

$$\frac{\partial U_i}{\partial t} = \mu \frac{\partial^2}{\partial x_j \partial x_j} \left(\frac{U_i}{\rho} \right) + \rho g_i - \frac{\partial}{\partial x_j} \left(\frac{U_i U_j}{\rho} \right) - \frac{\partial P}{\partial x_i} \quad (6)$$

where the pressure is calculated diagnostically from the Ideal Gas Law $P^{c_p/c_v} = R \Theta / P_0^{R/c_p}$ and δ slows the propagation speed of acoustic waves ($c = \sqrt{\gamma R T / \delta}$), allowing for longer time steps (Sun et al. 2012). R is the Universal Gas Constant divided by the mean molar mass of the fluid, and c_p and c_v are the appropriate specific heats at constant pressure and volume, respectively. The other variables are μ , the molecular viscosity; κ , the molecular conductivity; and g_i , the vector gravitational acceleration.

Using the prognostic density equation requires temporally resolving the acoustic waves; thus, simulations employ exceedingly small time steps for integration ($\sim 10^{-4} \tau^*$, the physical time scale). The simulations described in this study employed $\delta = 16$, thus stable integration is achieved using a time step 4 times larger than normally required without significantly impacting flow structures larger than a few times the grid spacing (Sun et al. 2012). A time-splitting scheme, where the more slowly varying forcing mechanisms are updated less often (e.g., Hsu and Sun 2001), is another alternative to decreasing the required computational resources.

The new model uses the quadratic upstream interpolation for convection kinetics (QUICK) finite-volume convection-diffusion scheme (Versteeg and Malalasekera 2007) modified to allow non-uniform grid spacing. The volume elements for the components of the momentum field are staggered with respect to the mass field (Arakawa C-grid). The volume elements are configured so that complete mass-field volume elements are in contact with the wall (Fig. 2). The outermost staggered velocity volume elements are between the 2 outermost mass-field cells in the direction of the velocity. In this configuration, no pressure boundary condition is

required for the momentum equation. Dirichlet boundary conditions are imposed on all prognostic fields.

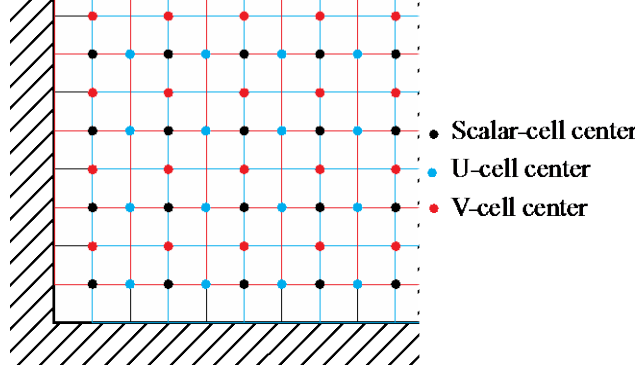


Fig. 2 Arakawa C-grid configuration in the xy -plane for the scalar mass field and the U- and V-components of the momentum field. The vertical momentum is staggered in the vertical direction from the mass field points.

Using the above semi-implicit scheme yields the following governing equations in Cartesian coordinates with fluxes computed on the surface of finite volume element:

$$\rho(\mathbf{x}, \Delta t + t_0) - \rho(\mathbf{x}, t_0) = -\frac{\Delta t}{\delta \Delta V} \sum_{i=1}^3 (\Delta S_i^{(+)} U_i^{(+)} - \Delta S_i^{(-)} U_i^{(-)}) \quad (7)$$

$$\begin{aligned} \theta(\mathbf{x}, \Delta t + t_0) - \theta(\mathbf{x}, t_0) = & \frac{\Delta t}{\Delta V} \sum_{j=1}^3 \left[\Delta S_j^{(-)} \left(\frac{\bar{u}_j^{(-)} \langle \theta \rangle^{(-)}}{\bar{\rho}^{(-)}} - \kappa \frac{\partial \langle \theta \rangle^{(-)}}{\partial x_j \bar{\rho}^{(-)}} \right) + \right. \\ & \left. \Delta S_j^{(+)} \left(\kappa \frac{\partial \langle \theta \rangle^{(+)}}{\partial x_j \bar{\rho}^{(+)}} - \frac{\bar{u}_j^{(+)} \langle \theta \rangle^{(+)}}{\bar{\rho}^{(+)}} \right) \right] \end{aligned} \quad (8)$$

$$\begin{aligned} U_i(\mathbf{x}, \Delta t + t_0) - U_i(\mathbf{x}, t_0) = & \frac{\Delta t}{\Delta V} \sum_{j=1}^3 \left[\Delta S_j^{(-)} \left(\frac{\bar{u}_j^{(-)} \langle U_i \rangle^{(-)}}{\bar{\rho}^{(-)}} - \mu \frac{\partial \langle U_i \rangle^{(-)}}{\partial x_j \bar{\rho}^{(-)}} \right) + \right. \\ & \left. \Delta S_j^{(+)} \left(\mu \frac{\partial \langle U_i \rangle^{(+)}}{\partial x_j \bar{\rho}^{(+)}} - \frac{\bar{u}_j^{(+)} \langle U_i \rangle^{(+)}}{\bar{\rho}^{(+)}} \right) \right] + \Delta t \bar{\rho} g_i - \frac{\Delta t}{\Delta V} (P^{(+)} \Delta S_i^{(+)} - P^{(-)} \Delta S_i^{(-)}) \end{aligned} \quad (9)$$

where the indices, $i, j=1, 2, 3$, indicate the vector components and cell faces in each direction. The superscripts (+) and (-) indicate values on the cell faces in the positive or negative direction from the cell center; $\Delta S_i^{(+)}$ and $\Delta S_i^{(-)}$ are the surface elements of the cell faces in the i -direction. With the staggered grid, the momentum flux contributions in the continuity equation and the pressure gradient term in the momentum equation are directly calculated rather than using interpolated values. Two types of interpolation are used for the convection-diffusion terms. An over bar indicates simple linear averaging between grid cell centers, if necessary; because

of the cell staggering employed, not all faces will require interpolation to find values on the faces. The $\langle \rangle$ operator indicates quadratic, upwind-weighted interpolation between surrounding cell centers in the direction of the flow through the face, as discussed in Versteeg and Malalasekera (2007).

The integration process is described using the above equations:

- 1) Using the discretized momentum equation (Eq. 9), calculate $\frac{\partial U}{\partial t}\bigg|_{t=t_0}$ in order to estimate the half-step momentum, $U_i(\mathbf{x}, t_0 + \frac{\Delta t}{2})$.
- 2) With the half-step momentum, advance the density a full time step (Eq. 7), and calculate the half-step density as a linear average between the old and updated densities.
- 3) The density-coupled potential temperature is then advanced by a half time step using the first-order Taylor expansion; the full-time-step advancement follows employing the updated mid-time-step density and density-coupled potential temperature.
- 4) With the updated scalar quantities, the mid-time-step pressure is calculated, and the momentum equation is advanced to the next full time step.
- 5) Finally, as recommended in Sun (2011), a light application of fourth-order Shuman smoothing (e.g., Haltiner and Williams [1980] or Shapiro [1975]) eliminates short-wave instability.

We found stable time integration for all simulations using 20% of the maximum smoothing coefficient and smoothing every 16 time steps.

3. Results

The ABLE model, using the above governing equations, simulated 3-D lid-driven cavity flow; results are compared with the laboratory measurements of Prasad and Koseff (1989). We specifically looked at the cases where the stream-wise, span-wise and vertical lengths were all equal (SOR=1) and Reynolds numbers were $Re=1000$, $Re=3200$, and $Re=10,000$. The results are normalized by the flow scales: the length scale, L , is the cube width; the velocity scale, U_0 , is the speed of the moving, upper lid; and the time scale is $\tau = L/U_0$.

3.1 Discretization Error

The theoretical accuracy of the numerical schemes has been derived in Sun (2011) and Versteeg and Malalasekera (2007) as second-order accurate in time and, when

using the QUICK scheme, third-order accurate in space. As implemented in the model source code, the spatial accuracy decreases due to the boundary condition treatment in both the convection-diffusion scheme and the smoothing routine.

The temporal accuracy was measured by simulating cavity flow for $Re=10,000$ using a mesh with $304 \times 304 \times 304$ grid points. The simulation used $\delta=16$ for a 4 times reduction in the speed of sound; the largest time step satisfied the Courant-Freidrichs-Levy (CFL) criterion for the slowed acoustic waves with a value of $5.8 \times 10^{-5} \tau$. Three additional simulations were performed using time steps of $1/2$, $1/4$, and $1/8$ of the largest time step. The L_2 -norm of the difference between each simulation and the simulation with the smallest time step taken at $t=5.8\tau$ (10^5 iterations of the largest timestep) is shown in Fig. 3 along with the line representing second-order accuracy in time.

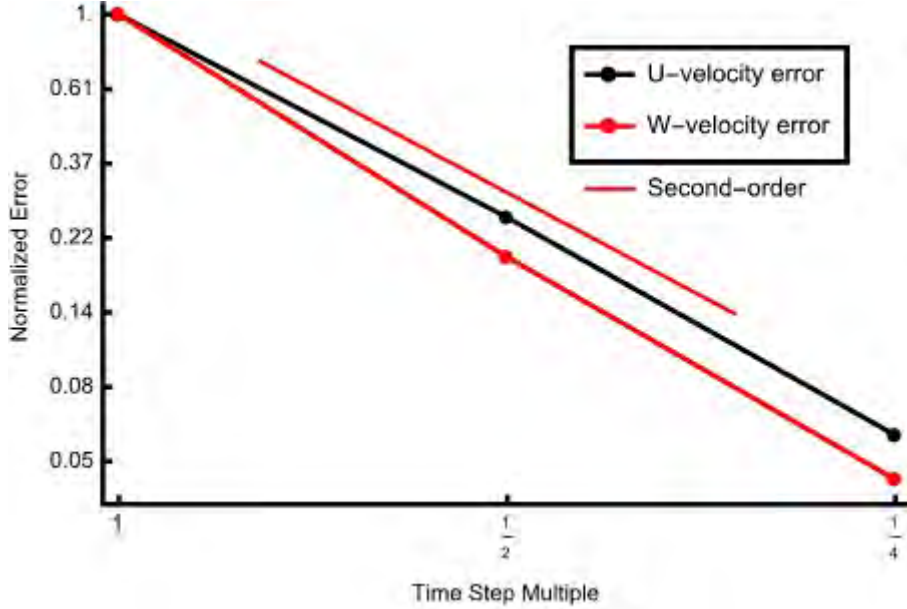


Fig. 3 Estimate of temporal discretization error based on lid-driven cavity flow simulations with $Re=10,000$. The largest time step satisfied the CFL criterion for the reduced speed acoustic waves. Additional simulations were performed using an identical grid, but with time steps reduced by factors of $1/2$, $1/4$, and $1/8$, which was used as the reference state.

For the spatial error estimates, simulations were performed with $Re=1000$ to reduce the computational requirements. The QUICK scheme is third-order accurate in space. However, the boundary condition treatment for both the convection-diffusion scheme and the explicit smoothing degrades the accuracy. Four simulations with differing grid spacings were performed; 75, 150, 300, and 450 grid points were used in each Cartesian direction. The time steps for all of the simulations were set at the time step satisfying the CFL criterion for the 450-grid point mesh, and the simulations were allowed to integrate $t=40\tau$ ($\sim 10^6$ time steps).

The coarser resolution simulations were compared with the finest resolution using third-order splines to interpolate between grid points. Mean absolute error of the difference between the interpolated values and the 450-grid-point simulation were then calculated over the area at the same physical time, $t=40\tau$, and plotted in Fig. 4.

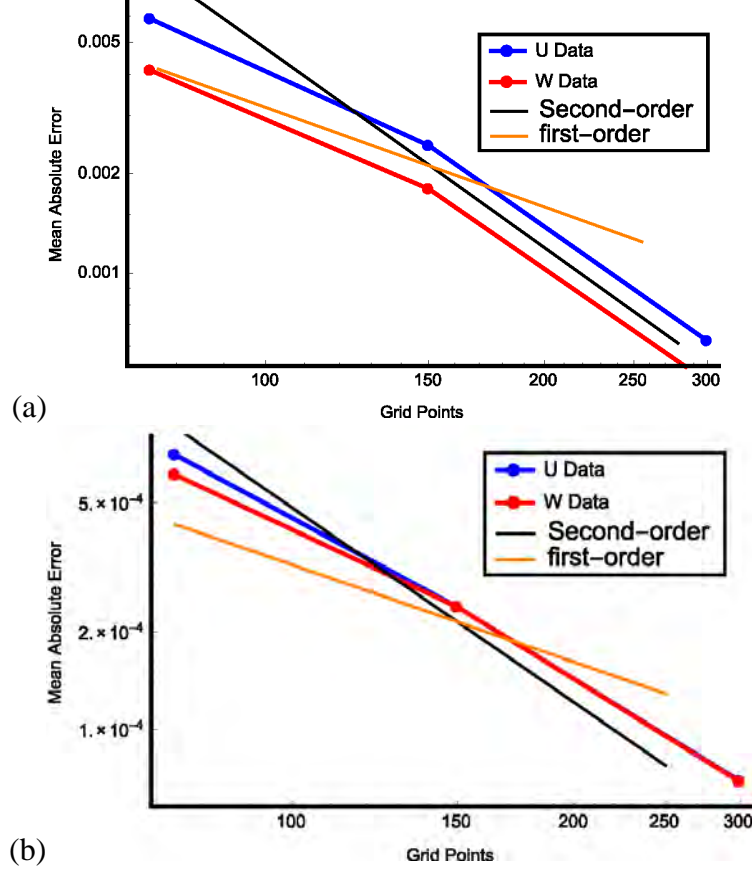


Fig. 4 Spatial discretization error estimates using stream-wise and vertical velocities in the plane of symmetry ($y=0$) for $Re=1000$. The error is the L_2 -norm of the variable difference from a reference simulation that used 450 grid points in each direction. For a) the error is calculated over the entire symmetry plane and for b) 20% of each side of the symmetry plane is excluded.

The error estimates are calculated for the stream-wise and vertical velocities for 2 regions of the central symmetry plane ($y=0$). The first region is the complete xz-slice through the center of the computational domain. The second region excludes 20% of the grid points along each boundary. Comparing Fig. 4a and 4b, it is readily apparent that most of the error results from the boundary condition treatment; the larger magnitude of the upper boundary condition of the u -velocity contributes more to the mean absolute error. The QUICK scheme is a third-order scheme, but the second-order treatments for both convection-diffusion and second-order smoothing at the wall boundaries degrades the discretization error to match second order in space.

3.2 Comparison with Simulation and Observations

The simulations were conducted as DNSs requiring high resolution in order to resolve motions into the dissipation sub-range: at least 75, 200, and 300 grid points in each direction for $Re=1000$, $Re=3200$, and $Re=10,000$, respectively. Gravity was disabled for these simulations and the potential temperature was fixed.

For $Re=1000$, the new model simulations are compared with the simulation data of Ku, Hirsh, and Taylor (1987), which employed a spectral DNS to solve for the 3-D flow field. Their 3-D simulations showed a significant change in the profile when compared with the horizontal and vertical centerline velocity profiles generated using 2-dimensional (2-D) simulations. Fig. 5 shows the stream-wise velocity along the central vertical axis of the symmetry plane and the vertical velocity along the central horizontal axis. All the simulations were in close agreement with the simulations of Ku, Hirsh, and Taylor (1987).

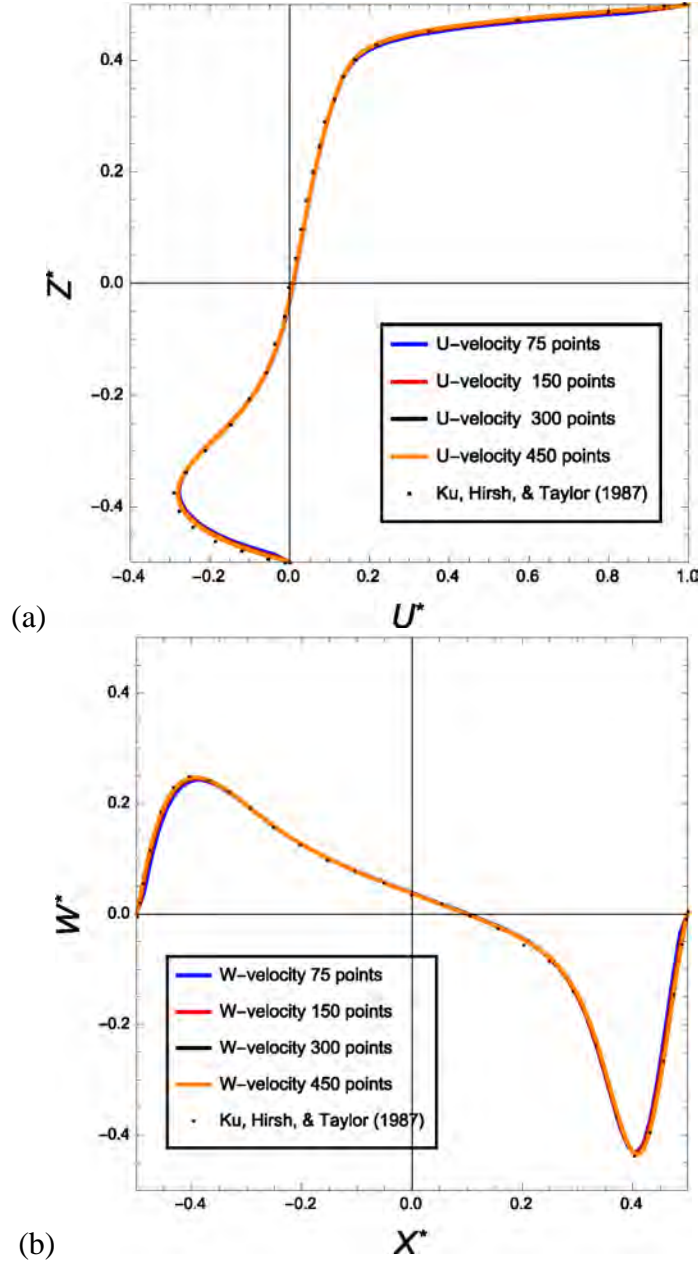


Fig. 5 a) Stream-wise velocity along the central vertical axis and b) vertical velocity along the central horizontal axis for $Re=1000$. The model simulations used 75, 150, 300, and 450 grid points in each direction and are compared with the simulations of Ku, Hirsh, and Taylor (1987).

The simulations at higher Reynolds number ($Re = 3200$ and $Re = 10,000$) are verified against the laboratory observations of Prasad and Koseff (1989). For better comparison with the statistics of the Doppler velocimetry observations, the points along the central vertical axis in the symmetry plane ($x = y = 0$) and the central horizontal axis ($y = z = 0$) in the symmetry plane were written for every time step,

which was $\sim 10^{-4}\tau$ ($Re=3200$) and $\sim 5 \times 10^{-5}\tau$ ($Re=10,000$). For both cases, the model was integrated for a physical time of approximately 120τ .

A representative sample of the evolution of the flow for $Re=3200$ is shown in the density and streamline plots of Fig. 6. The simulation was allowed to achieve quasi-steady-state, which exhibited a periodic shedding of the downstream secondary eddy (DSE) and the upstream secondary eddy (USE) (see Fig. 1). The flow shows the prototypical state with a large primary eddy (PE) and well-defined secondary eddies—the DSE, the USE, and a small deviation for the upper upstream eddy (UUE) (see Fig. 1). The DSE is then shed into the primary flow, causing the downstream flow to wrap around the PE further from the lower wall. As the DSE is absorbed into the PE and USE is shed into the primary circulation, the upward flow near the bottom boundary weakens, leading to a rapid drop in the level that the downstream flow becomes horizontal. This drop is associated with an acceleration of the downstream flow, which reestablishes the DSE and then the USE. For the higher- Re flow, there is a similar DSE and USE shedding process; the spike in the vertical velocity variance is lower magnitude and narrower due to the decreased viscous diffusion.

The flow took approximately 35τ to achieve quasi-steady-state, which forms the lower boundary of the window used to calculate the mean and second-order statistics. Comparing the simulation results to the observations, we see excellent agreement with the mean features (Fig. 7). The sharp gradients in the mean field, especially near the walls, are well represented. The downstream flow (near the right wall) is highly localized in both simulations, with the expected wider profile for the lower- Re flow.

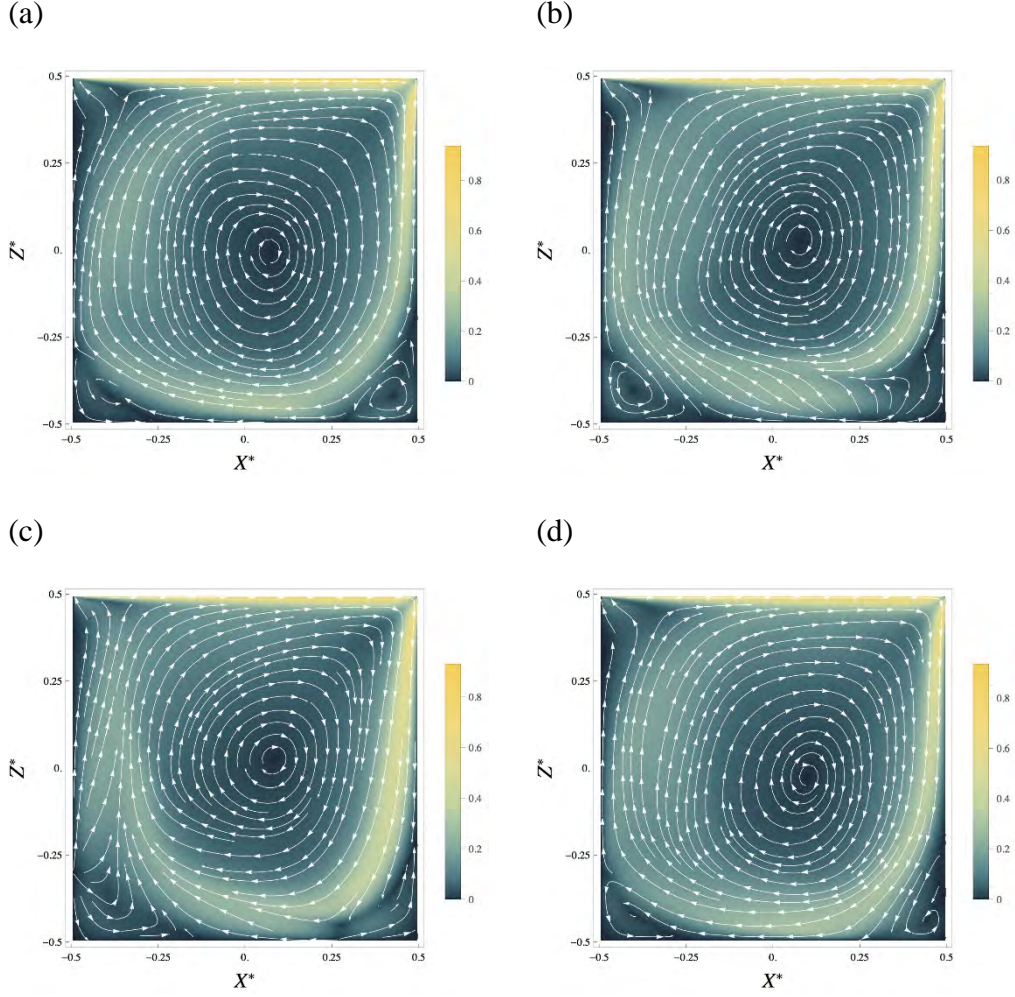


Fig. 6 Streamlines and UW-velocity magnitudes ($Re=3200$) showing a) at $t = 90\tau$, a well-defined DSE and localized downstream flow along the right, boundary; b) at $t = 93\tau$, the shedding of the DSE raising the level that the downstream maximum wraps around the PE; c) at $t = 97\tau$, drop and acceleration of the downstream flow; and d) at $t = 104\tau$, reestablishment of the DSE and thinning of the downstream maximum.

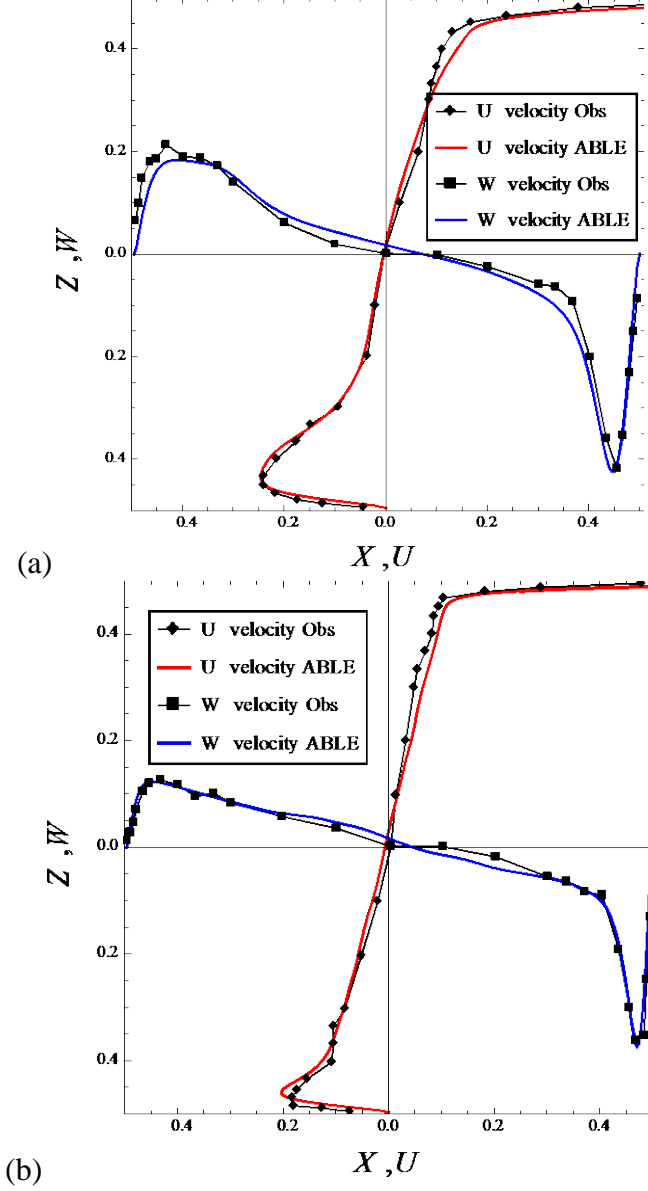


Fig. 7 Non-dimensional mean horizontal and vertical velocity fields along the x- and z-axes in the symmetry plane ($y=0$) for a) $Re=3200$ and b) $Re=10,000$

The features of the velocity variances (Fig. 8, scaled for clarity) also capture the observed behavior described by Prasad and Koseff (1989). The high-peaks in the vertical velocity variance near the right lateral boundary are associated with the thickening and thinning of the high-velocity shear layer associated with the shedding of the DSE vortex in the corner described above. Using a lower order convection-diffusion scheme (such as upwind-differencing) with excessive numerical diffusion did generate the secondary vortices; however, the shedding process was eliminated. The flow, instead, generated a stable PE with steady DSE and USE. The shedding of the DSE (and USE) has impacts as discussed in Prasad

and Koseff (1989): 1) sharp increase in the velocity variance along the lower boundary due to said eddies crossing the centerline and 2) the thickening and thinning of the high-velocity downward boundary layer along the vertical wall on the downstream side, appearing as a spike in the vertical velocity variance. The greater turbulent diffusion associated with the higher-Re flow leads to a less localized increase in the horizontal velocity variance along the bottom boundary.

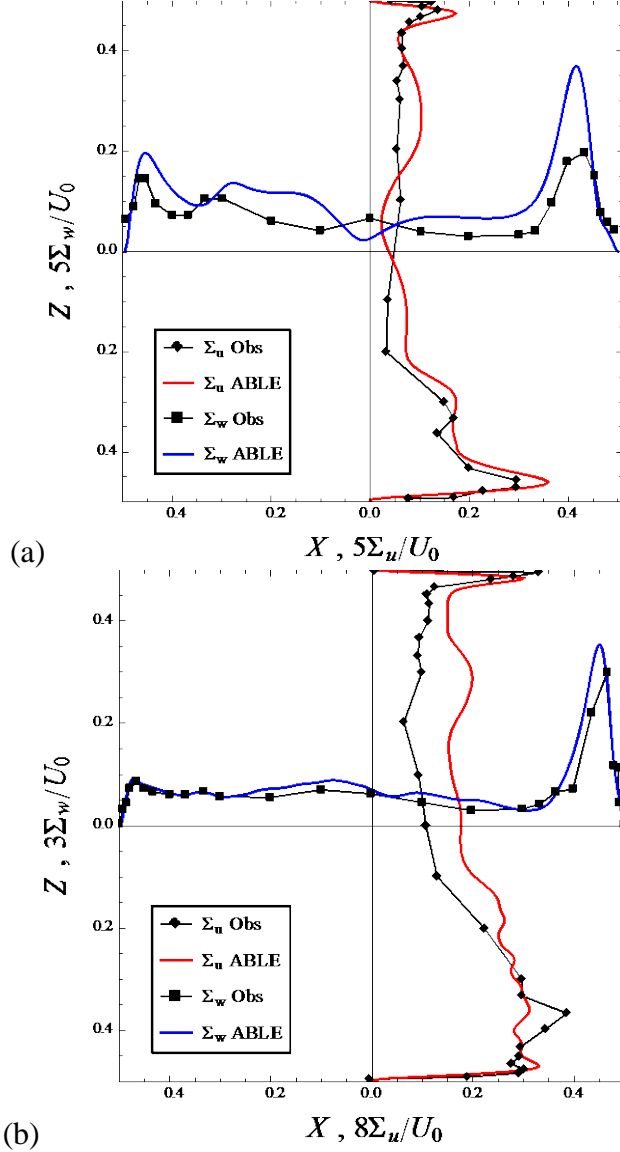


Fig. 8 Scaled horizontal and vertical velocity variances along the x- and z-axes in the symmetry plane ($y=0$) for a) $Re=3200$ and b) $Re=10,000$

The effect of the shedding of the DSE and USE also has significant effect on the velocity covariances (Fig. 9, scaled for clarity) producing a large positive value along the right lateral boundary. An increase in downward velocity ($-w'$) is associated with the thickening (in the negative x-direction) for the downstream flow

(-u'). Similarly, the slowing of the flow (+w') is associated with the rightward motion, thinning the downstream flow (+u').

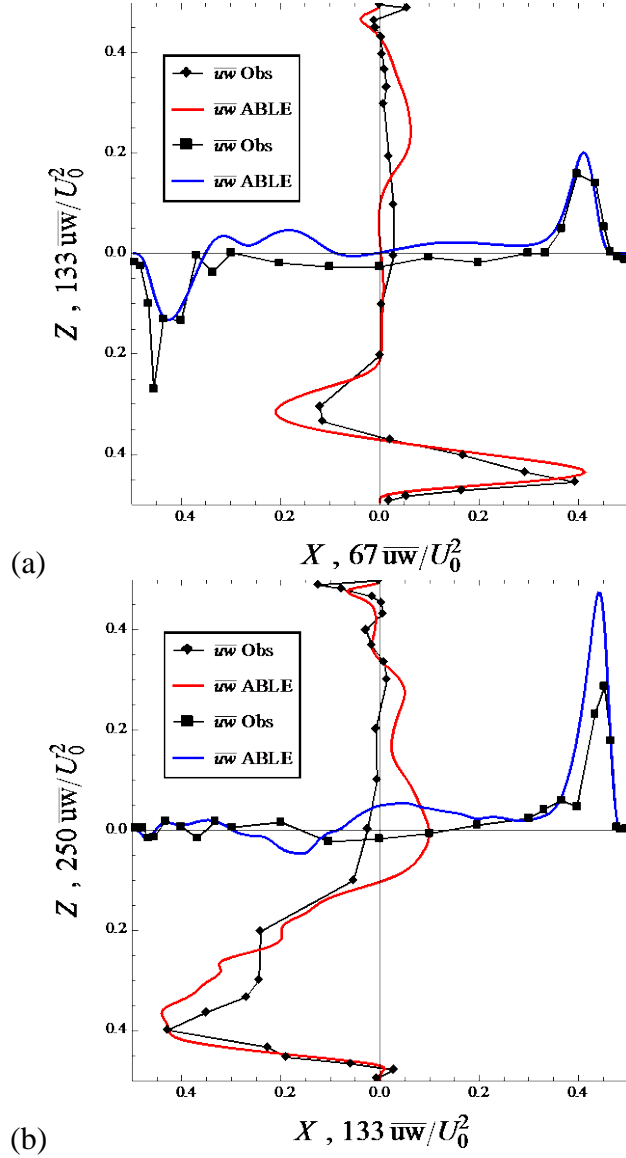


Fig. 9 Scaled horizontal and vertical velocity covariances along the central axes in the symmetry plane ($y=0$) for a) $Re=3200$ and b) $Re=10,000$

The large positive peak in the $\overline{u'w'}$ -covariance near the bottom boundary for the low- Re simulation was described in Prasad and Koseff (1989) as being caused by the meandering of the Taylor-Goertler-like (TGL) vortices on the $Re=3200$ flow (Fig. 10). As the TGL vortices approach the symmetry plane, the vertical velocity increases, and the horizontal velocity maximum moves upwards, yielding a decrease in the negative, x-component of the velocity (i.e., +u') relative to the mean near the surface boundary, and an increase in the negative U-velocity above

(i.e., $-u'$). Coupled with the upward motion ($+w'$), the movement of the TGL vortices close to the symmetry plane contributes to a sharp positive increase in the \overline{uw} -covariance below the mean U-velocity maximum. Above the mean U-velocity maximum, the covariance will exhibit a negative peak. The observations from Prasad and Koseff (1989) show a meandering period of about 70τ , whereas the simulations showed a much smaller meandering period of approximately 14τ .

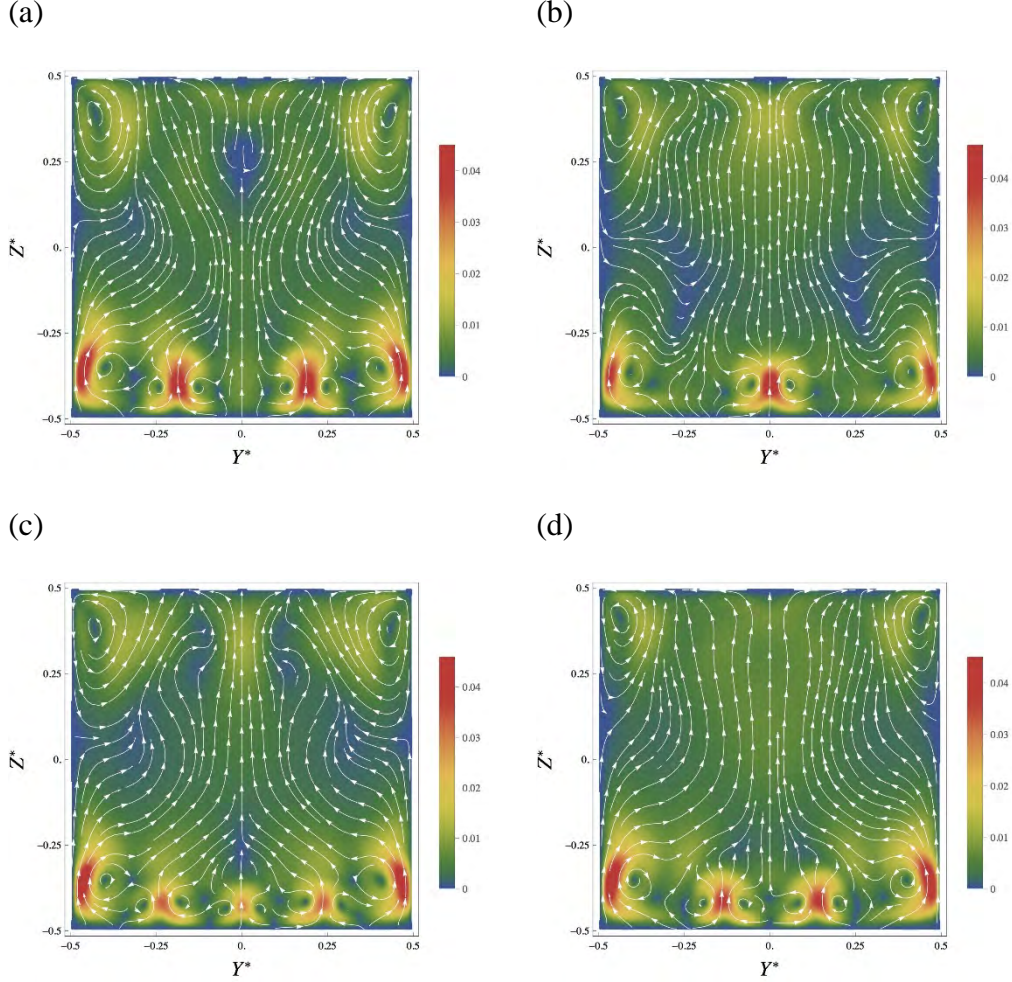


Fig. 10 Streamline and VW-velocity magnitudes for the same times shown in Fig. 6 a) $t = 90\tau$, b) $t = 93\tau$, c) $t = 97\tau$, and d) $t = 104\tau$. This progression of figures shows the meandering of the TGL vortices near the symmetry plane ($Y^*=0$).

For the $Re=10,000$ flow, the TGL vortices have a less regular configuration and are transient (Fig. 11). In addition, the mean U-velocity maximum is closer to the lower boundary. There is a small positive incursion in the \overline{uw} -covariance near the lower boundary; however, during DSE shedding events most of the lower part of the domain experiences negative x-acceleration (increase in negative U-velocity), with

an increase in the upward component or a positive x-acceleration (decrease in negative U-velocity) during the downward shift of the velocity maximum.

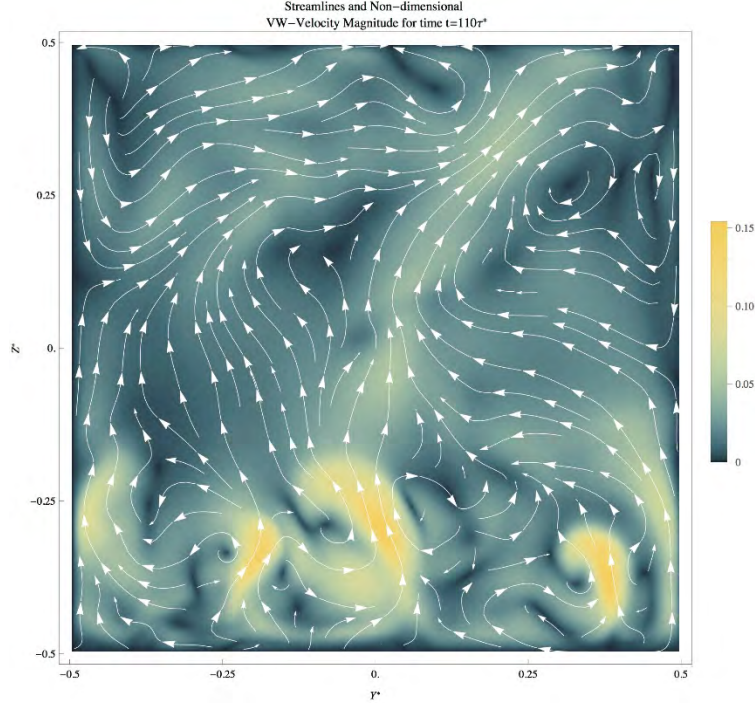


Fig. 11 Streamlines and VW-velocity magnitude for $Re=10,000$ at time, $t = 110\tau$. For the higher- Re flow the vortices generated near the lower boundary are irregular and transient.

4. Conclusion

We extended the time integration scheme of Sun (2011) to 3-D Navier-Stokes and implemented the scheme in the ABLE model. The scheme was straightforward to implement and parallelize using Message Passing Interface (MPI) (optimizing ABLE for heterogeneous platforms (e.g., general purpose computing on a graphics processing unit [GPGPU] is in progress). The model showed favorable stability and fidelity characteristics when applied to lid-driven cavity flow at $Re=1000$, $Re=3200$, and $Re=10,000$. The simulations accurately reproduced the mean velocity fields and the second-order statistics along the symmetry plane ($y=0$) when compared with other 3-D simulations of Ku, Hirsh, and Taylor (1987) and the laboratory observations of Prasad and Koseff (1989). The initially imposed, random perturbations in the density field (initially, $\sim 10^{-5}\rho_0$) are maintained because of the lower numerical diffusion, despite the smooth nature of the boundary conditions, the use of Shuman smoothing to control short-wave instability, and the small time steps required. Maintaining small random perturbations in the flow preserved the transient nature of the flow structures, such as the formation and shedding of the DSE, USE, and TGL vortices. Associated with the shedding of the corner eddies is

the alternating thickening and thinning of the lateral boundary layer, leading to the spikes in the vertical velocity variance, σ_w , above the DSE and above the lower boundary. The production and meandering of TGL vortices in the $Re=3200$ flow leads to a large positive value for the \overline{uw} -covariance, as observed in the laboratory.

5. References

- Chimonas, G. Steps, waves and turbulence in the stably stratified planetary boundary layer. *Boundary Layer Meteorology*. 1999;90:397–421.
- Grubišić V, Doyle JD, Kuettner J, Poulos GS, Whiteman CD. T-REX Terrain-Induced Rotor Experiment Overview Document and Experimental Design. 2004
- Haltiner GJ, Williams RT. Numerical prediction and dynamic meteorology. John Wiley and Sons, Inc., 2nd edition;1980.
- Hsu W-R, Sun W-Y. A time-split, forward-backward numerical model for solving a nonhydrostatic and compressible system of equations. *TELLUS*. 2001;53A:279–299.
- Moeng CH, Sullivan P. A comparison of shear- and buoyancy- driven planetary boundary layer flows. *J. Atmos. Sci.* 1994;51:999–1022.
- Prasad AK, Koseff JR. Reynolds number and end-wall effects on a lid-driven cavity flow. *Physics of Fluids A*. 1989;1(2):208–218.
- Shankar P, Deshpande M. Fluid mechanics in the driven cavity. *Annual Review of Fluid Mechanics*. 2000;32:93–136.
- Shapiro R. Linear filtering. *Mathematics of Computation*. 1975;29(132):1094–1097.
- Sun W-Y. Instability in leapfrog and forward-backward schemes. *Monthly Weather Review*. 2010;138:1497–1501.
- Sun W-Y. Instability in leapfrog and forward-backward schemes part ii: Numerical simulations of dam break. *Computers and Fluids*. 2011;45:70–76.
- Sun W-Y, Sun OM, Tsuboki K. A modified atmospheric non-hydrostatic model on low aspect ratio grids. *Tellus*. 2012;64.
- Versteeg HK, Malalasekera W. *An Introduction to Computational Fluid Dynamics: The Finite Volume Method*. Pearson Prentice Hall, 2nd edition;2007.
- Wang Y, Williamson C, MacCall B. A description of the framework of the atmospheric boundary layer environment (ABLE) model. Adelphi (MD): Army Research Laboratory (US); 2012. Report No.: ARL-TR-6177.

List of Symbols, Abbreviations, and Acronyms

2-D	2-dimensional
3-D	three-dimensional
ABLE	Atmospheric Boundary Layer Environment
CFD	computational fluid dynamics
CFL	Courant-Freidrichs-Levy
DNS	direct numerical simulation
DSE	downstream secondary eddy
DSRC	Defense Shared Resource Centers
GPGPU	general purpose computing on a graphics processing unit
HPC	high-performance computing
HPCMO	High-Performance Computing Modernization Office
MPI	Message Passing Interface
PBL	planetary boundary layer
PE	primary eddy
QUICK	quadratic upstream interpolation for convective kinetics
TGL	Taylor-Goertler like
USE	upstream secondary eddy
UUE	upstream upper eddy

- 1 DEFENSE TECH INFO CTR
(PDF) DTIC OCA
- 2 US ARMY RSRCH LAB
(PDF) IMAL HRA MAIL & RECORDS MGMT
RDRL CIO LL TECHL LIB
- 1 GOVT PRNTG OFC
(PDF) A MALHOTRA
- 2 US ARMY RSRCH LAB
(PDF) RDRL CIE D
B MACCALL
Y WANG